École polytechnique de Louvain

Main title of the master thesis (possibly split on several lines)

Optional subtitle

Author: **Michele Cerra**
Supervisor: **Benoît Macq**
Reader: **Alexandre Berger**

Academic year 2022–2023
Master [120] in Computer Science and Engineering

Abstract

Acknowledgments

Contents

Introduction

Chapter 1

Theoretical background

1.1 Magnetic Resonance Imaging

1.1.1 Magnetic properties of nuclei

Biological organisms and tissues are naturally abundant of *Hydrogen* atoms, mostly in water and fats. Thanks to the magnetic properties of Hydrogen atoms it is possible to build anatomical images of the human body.

From a classical point of view an atomic nucleus can be assumed as sphere rotating around its axis 1.1a. This rotation is called spin and it is a fundamental property of nucleus. The *spin* is the intrinsic angular momentum of the nucleus and can be an integer or a half-integer depending of the mass number[1] and the atomic number[2]. In the particular case of the Hydrogen it is present only a proton and the spin can take only tha values $1/2$ and $-1/2$.
Since the nucleus is a charged particle, a rotation of it creates a magnetic field. From this point of view the particle behaves like a small magnetic dipole 1.1a: $\vec{\mu} = i\vec{S}$ where $\vec{\mu}$ is the intrinsic magnetic momentum that is aligned on its spin $\vec{S}$.

[1]Mass number: number of protons and neutrons
[2]Atomic number: number of protons

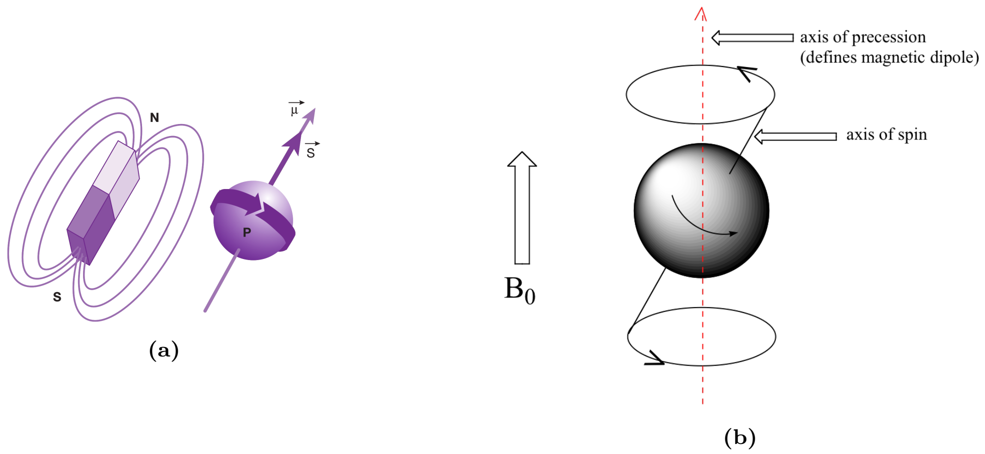

Figure 1.1: (a) Representation of the spin and the magnetic moment. [B. Kastler, 1988], (b) Precessional motion of a proton spin in an applied magnetic field. [Kennepohl D., 2019]

Normally orientation of $\vec{\mu}$ is completely random due to thermal random motion, therefore the sum of the magnetic fields is null ($\sum_i \mu_i = 0$).
In a magnetic dipole, when an external magnetic field $\vec{B_0}$ is applied, the individual orientation can take two possible orientations: *parallel* or *anti-parallel*. This phenomena in the particles is different, since the particle is rotating, the external magnetic field creates a *precession* around $\vec{B_0}$ like a spinning top 1.1b: $\vec{\Gamma} = \vec{\mu} \times \vec{B_0}$ where $\vec{\Gamma}$ is the *torque*. The axis rotates around the area of a "cone", with an angular speed proportional to the applied field following the *Larmor's Law*:

$$f_0 = \frac{\gamma}{2\pi} B_0 \tag{1.1}$$

γ is the gyromagnetic ratio and it is a characteristic of the nucleus. The frequency of precession is called *Larmor frequency*.
From a global point of view, the populations of protons moments create a macroscopic magnetization, with the direction equal to the external field 1.2.

$$\vec{M} = \frac{1}{V} \sum_i \vec{\mu_i} \tag{1.2}$$

While the transversal magnetization in xy plane is null, since the components μ_{xy} rotate with different phases and overall they nullifying themselves 1.2.

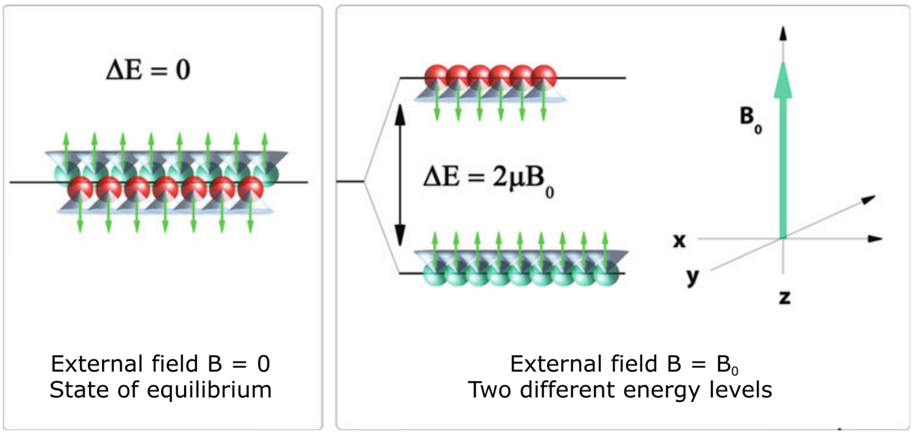

Figure 1.2: Separation of different energy levels after the application of the external field B_0. The population of spins in the lower level is slightly more of the upper.[O. Rampado, 2017] Translated.

In terms of energy, without the magnetic field, it doesn't exists any difference between the two orientations (parallel and anti-parallel), because them are equiprobable. With the application of the static magnetic field the anti-parallel orientation will have an higher energy ($N \downarrow$) than the parallel with lower energy ($N \uparrow$), since it has to be the opposite of the external field. The *occupation ratio* of the two energy levels is described by the *Boltzmann distribution*.

$$\frac{N_\uparrow}{N_\downarrow} = e^{-\frac{\Delta E}{kT}} \tag{1.3}$$

where k is the Boltzmann's constant and T is the absolute temperature in [K].
The energy of a magnetic dipole in a magnetic field $\vec{B_0}$ can be defined by:

$$E = -\vec{\mu} \cdot \vec{B_0} = -\mu_z B_0 \Rightarrow$$

where $\mu_z = \gamma \frac{h}{2\pi} I$

$$\Rightarrow E_I = -\gamma \frac{h}{2\pi} I B_0$$

where h is the Planck's constant and I is the spin orientation for the Hydrogen. Knowing that:

$$\Delta E = E_{-\frac{1}{2}} - E_{\frac{1}{2}} = h \frac{\gamma}{2\pi} B_0 = h f_0$$

we find that there are more spins in $E_{\uparrow}$ (lower energy) state than $E_{\downarrow}$ (higher energy) state 1.2.
The equilibrium macroscopic magnetization is non-zero and is defined by:

$$M_0 = \frac{(\frac{\gamma}{2\pi})^2 h^2 \rho B_0 I(I+1)}{3kT} \tag{1.4}$$

where ρ is the spin density[3] and $I = 1/2$ for Hydrogen.

1.1.2 Radiofrequency pulse

Since the intensity of the macroscopic magnetization (M_0) is several orders of magnitude smaller than the main field (B_0), is impossible to measure it directly[4].
The idea is to induce controlled oscillations of the spin system in order to generate a measurable signal. If a RF pulse is applied at the Larmor frequency ($f_{RF} = f_0$) we observe a *condition of resonance* 1.3, and if the system resonates with the pulse it starts to absorb energy 1.4.

$$B_1(t) = 2B_1(t)\cos(2\pi f_{RF} t + \phi)\vec{1}_{xy} \tag{1.5}$$

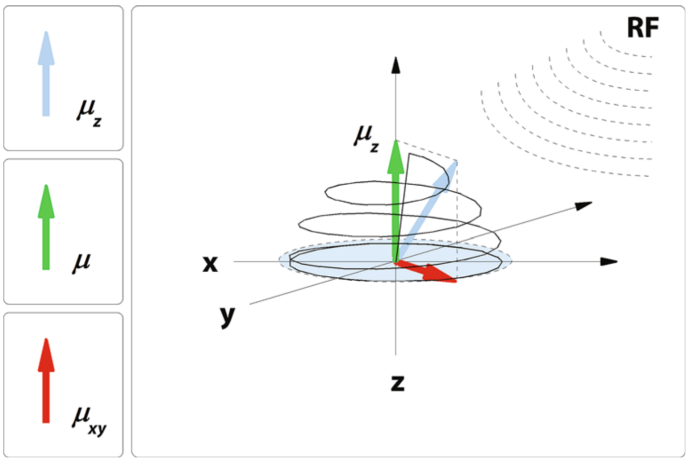

Figure 1.3: Trajectory of the magnetization vector. The vector describes a spiral trajectory by rotating at the Larmor frequency, tilting more and more, until it gets to rotate on the transverse plane. [O. Rampado, 2017]

[3]Spin density: number of spins per unit volume

[4]Even if is impossible to measure directly the M_0, it is proportional to the field, therefore an higher B_0 allows to generate higher signals with higher SNR and less acquisition times.

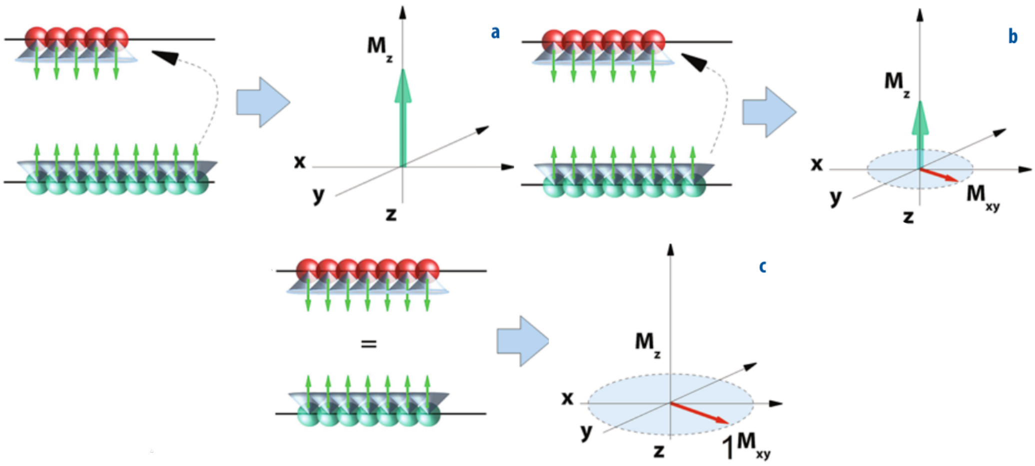

Figure 1.4: Effect of the RF impulse. (a) Initial situation; (b) System during the impulse; (c) System after 90 RF impulse. [O. Rampado, 2017] Arranged.

The *flip angle* from the initial direction of the magnetization is defined by:

$$\theta = \gamma B_1 T_{RF}$$

where T_{RF} is the duration of the RF-pulse.
Now the magnetization vector can be represented with a longitudinal magnetization M_z and a transverse magnetization M_{xy}:

$$\vec{M} = M_z \vec{1_z} + M_{xz} \vec{1_{xy}} \tag{1.6}$$

1.1.3 Relaxation

After applying the RF-pulse tends to go back to the initial state, these phenomena are called *relaxation*.

$$M_z \to M_0$$

$$M_{xy} \to 0$$

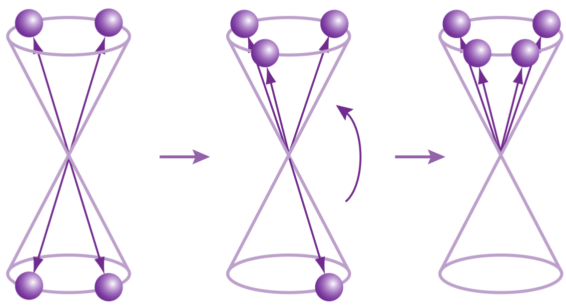

Figure 1.5: There is a progressively transition to the equilibrium from the high level to the lower lever of energy. [B. Kastler, 1988]

The first is the *longitudinal relaxation* (*spin-lattice relaxation* or *T1-relaxation*) in which the magnetization recovers to its original M_0, because the energy state after the RF-pulse is unstable it will create a transition of spins from high energy to low energy 1.5.

$$M_z(t) = M_0 + (M_z(0) - M_0)e^{-\frac{t}{T_1}} \tag{1.7}$$

where T_1 is the time needed to M_z to reach the 63% of the initial value M_0 1.6.

In the T_1-weighted image the signals must depend on the T_1 relaxation. Therefore the time between the RF-pulses have to be brief, but sufficient to differentiate the different tissues 1.6. In these scans, the white matter is represented in light grey, the grey matter in a darker shade of grey and the fluids in black.

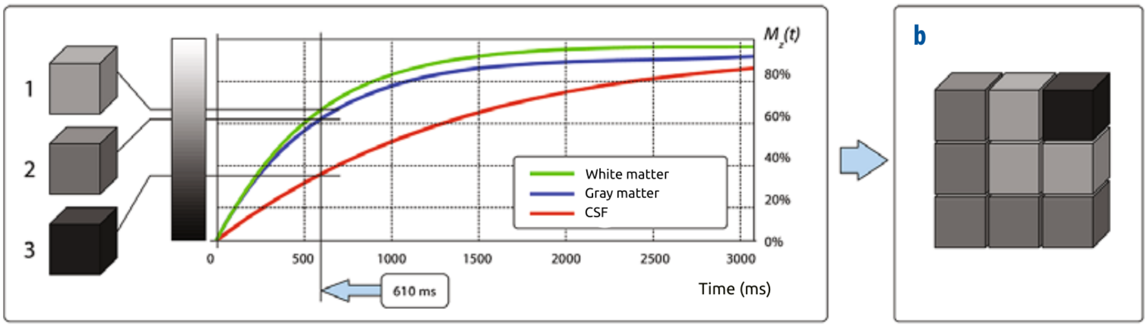

Figure 1.6: The T_1 relaxation time is different for type of tissues. [O. Rampado, 2017] Translated.

The second phenomenon is the *transverse relaxation* (*spin-spin relaxation* or *T2-relaxation*) and it is characterized by a loss in coherence of the spin phases 1.7.

$$M_{xy}(t) = M_{xy}(0)e^{-\frac{t}{T_2}} \tag{1.8}$$

where T_2 is the time needed to M_{xy} to reduce itself to 37% of the initial value 1.8.

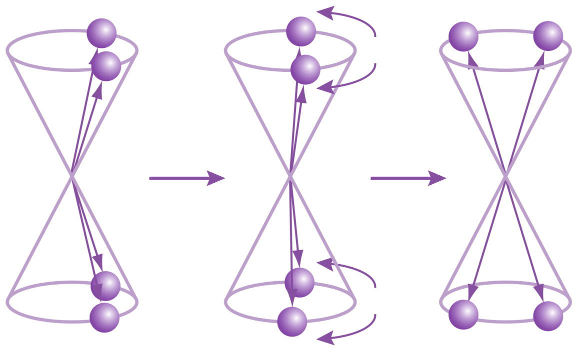

Figure 1.7: After the RF impulse there is a fast dephasing of the protons. The transversal magnetization M_{xy} decreases quickly. [B. Kastler, 1988]

In the T_2-weighted imaged the signals must depend only from the T_2 relaxation. Therefore is needed to wait that the T_1 relaxation effects are exhausted before reading the signal and send a new one. In these scans, the white matter is in dark grey, the grey matter is in light grey and the cerebrospinal fluid is in white 1.8.
In real conditions of an imperfect homogeneity of the field B_0 we see the *effective relaxation time*:

$$\frac{1}{T_2*} = \frac{1}{T_2} + \gamma \Delta B_0 \tag{1.9}$$

Where ΔB_0 are the inhomogeneities in the magnetic field.

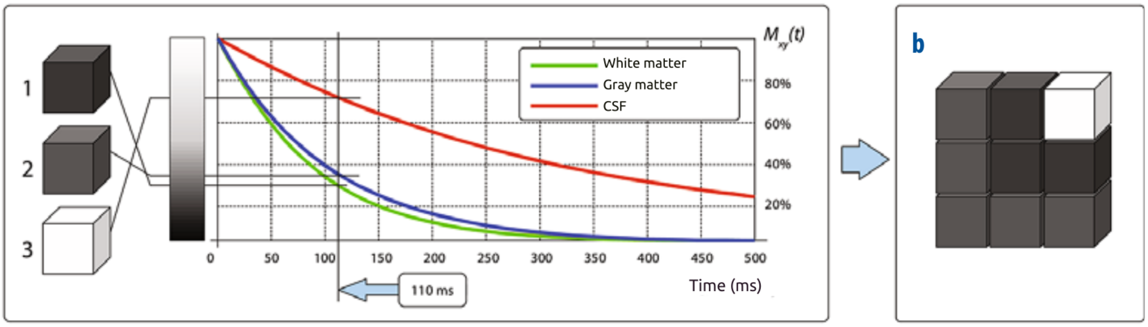

Figure 1.8: The T_2 relaxation time is different for type of tissues. [O. Rampado, 2017] Translated.

1.1.4 Spin-echo sequence

To obtain images with different type of contrast is needed to control the time between RF-pulses and the time of between readings of the signal.
The first sequence utilized for clinical purpose is the *spin-echo*. It introduces two main parameters: *Echo time* (TE) and the *Repetition time* (TR). The time between two 90° RF-pulses is defined ad TR, while the time between the RF-pulse and the first echo is defined as TE.
The strength of this sequence is the capacity of reading the T_2-weighted signals and not the T_2* 1.9.

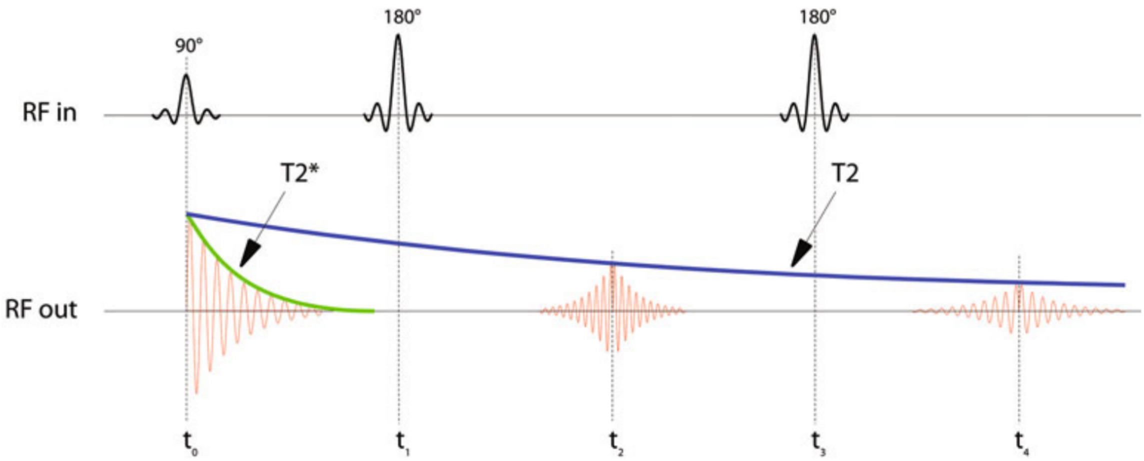

Figure 1.9: Recovering of the T_2-weighted signals from the T_2* through the Spin-echo sequence. The T_2-weighted signals is created by interpolating the peaks of the spin echo signals. The time between t_0 and t_2 is defined ad TE [O. Rampado, 2017]

The spin-echo sequence is composed of two type of RF-pulses: a 90° pulse and many 180° pulses. These last pulses have a double intensity and are called *echo impulses*. An echo impulse mirror all the spins of 180°, therefore the faster spins and the slower are inverted of position, creating the possibility that all the spins are refocused at time TE.

Contrast

By varying TE and TR, three types of contrast behavior can be obtained 1.11:

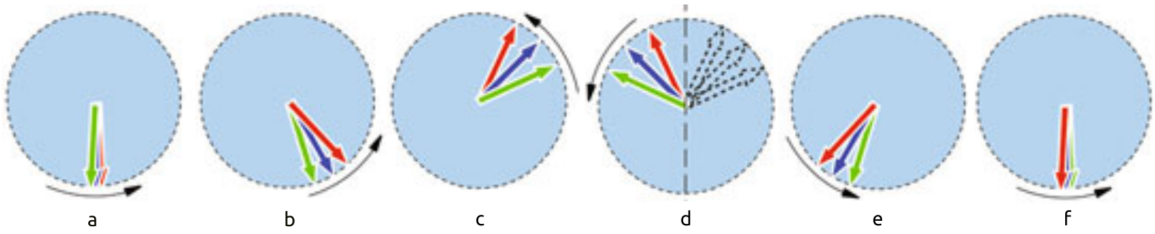

Figure 1.10: (a) After the end of the 90° RF impulse the protons are with the same phase. (b) The protons precession are different due to the inhomogeneities of the magnetic field. (c) The phases are completely different, there are some faster protons than others. (d) A 180° RF impulse move the proton position in a symmetric way in order to the slower protons are after the faster. (e) In the rotation the spins recover progressively the same phase. (f) At this time is generated a spin echo. [O. Rampado, 2017] Arranged.

- $TE << T_2$ and $TR = T_1$: T_1-contrast
- $TE = T_2$ and $TR >> T_1$: T_2-contrast
- $TE << T_2$ and $TR >> T_1$: ρ-contrast (proton density)

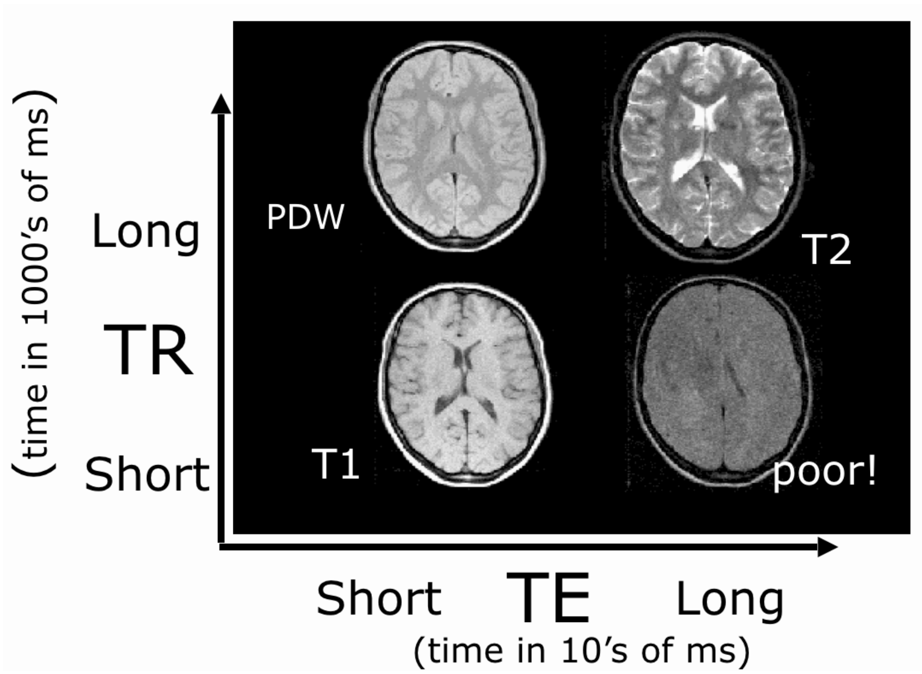

Figure 1.11: Matrix showing the different contrasts obtained with different TE and TR values. [Sameer, 2017]

1.1.5 Spatial coding

To reconstruct the image it is needed selecting a definite volume of tissue called *voxel*[5], three operations are needed to localize them in the tissue: selecting the layer (in the z-direction), selecting the column of the voxel (in the x-direction) and selecting

[5] A voxel is the 3D expansion of a pixel

the row (in the y-direction). These selections are done by linear variations of the magnetic field along a specific direction called *Gradient fields*. They can change the static magnetic field B_0 and thus change the precession frequency of protons.

To select a slice, it is applied a gradient along the z-direction, here the magnetic field change raising from a minimum to a maximum, and in the point in which the gradient is null the magnetic field is exactly B_0. Therefore only the nuclei in the condition of resonance will generate a signal 1.12.

Figure 1.12

Using a gradient on the x-direction (G_x) creates a signal that is the *sum of the associated signals with different frequencies*. This gradient is called *Gradient of frequency encoding*, because the spins assume a precession frequency depending on the gradient. Successively, is applied a gradient along the y-direction (G_y), called *Gradient of phase encoding*, it change the spin phase depending on the gradient 1.13. In this way each element of the section is different from the other by phase or frequency.

The raw data from these signals are collected in matrices that represent the *k-space* in the frequency domain, in which G_y selects the row and G_x scans it and save it in the matrix. This sequence must be repeated n times for each line of the k-space to fill it 1.13. After, is applied the *Inverse Fourier transform* to retrieve the image in the spacial domain.

Figure 1.13

1.1.6 Artifacts

In MRI artifacts is everything that is represented in the image without any correlation with the real anatomy of the tissues analyzed.

Motion artifacts

The most common artifacts are the *movement artifacts* due to the involuntary movements of the patient. In general the movements can be divided in random and periodic movements. Random movements create a blurring of the image, while periodic movements create *ghost images*[6]. The first can be reduced using techniques that reduce the acquisition time. The periodic movements artifacts can be reduced through *gating*, a technique where the acquisition of the data is synchronized with the periodic movement of the tissue.

Magnet susceptibility artifacts

The presence of ferromagnetic materials create local inhomogeneities in the magnetic field which result in distortion artifacts called *magnetic susceptibility artifacts*. The signals can change generating zone bright or dark with some distortions in the

[6]Ghost images: periodic copies of some structures of the image

surrounding tissues. These artifacts can be reduced using spin-echo sequence instead of gradient-echo, and reducing the TE.

Chemical shift

In the interface between tissues of different molecular characteristics can occur a *chemical shift*. It is a result of different resonance frequencies of adjacent tissues. Possible solutions are the reducing of the voxel dimension, increasing the bandwidth or using fat-suppressed imaging.

Gibb's artifacts

Gibb's artifacts are due to the reconstruction from k-space, since it is performed through a finite sampling. In hedges of high-contrast the Fourier transform truncate some frequencies, for this they are also named *truncation artifacts*, creating the effect of fine parallel lines ("ringing") adjacent to such interfaces. Increasing the matrix size or applying smoothing filters can reduce the artifacts.

Aliasing

Aliasing artifacts are visible when the tissue is outside the field-of-view (FOV), meaning that there was an under-sampling in the k-space. The only solution is to increase the size of the FOV or using techniques of foldover suppression.

Eddy currents

The Faraday-Lenz Law of electromagnetism states that electrical currents (*Eddy currents*) are induced in nearby conductors by a changing magnetic field. Since MRI uses rapidly changing magnetic fields, eddy currents are always produced. The conductive material in which eddy currents are induced may be any metallic component of the MRI scanner and the patient as a whole. These latter may generate a distortion of the magnetic field. Several techniques are available to minimize te effects including image post-processing [QeA,].

Figure 1.14

1.2 Diffusion-Weighted MRI

Sequences of *Diffusion-Weighted MRI* (DW-MRI) can provide motion-dependent contrast of water molecules in tissues, which can significantly alter in some brain diseases. This sequences are also know as *Diffusion Weighted Imaging* (DWI) or *diffusion MRI* (dMRI).

1.2.1 Pulse Gradient Spin Echo (PGSE)

The *Pulse Gradient Spin Echo* (PGSE) sequence is the main diffusion-weighted sequence used, it is composed of two magnetic gradients, before and after the 180° RF-pulse of the classic spin echo sequence. When the first diffusion gradient is applied, the water molecules are dephased, the second gradient, after the 180° RF pulse, will rephase the magnetization 1.15. The difference of gradient intensity which is subject the water molecule is proportional to the distance traveled on the time between the two gradients and also the gradient intensity. Therefore, the protons that are moved faster will have a greater dephase.

The intensity of a voxel can be described by the Stejskal-Tanner equation, in which the signal will be equal to the intensity of a T_2-weighted image, lowered by a quantity that depends on the diffusion of the molecules.

$$I = I_0 \cdot e^{-b_{PGSE} \cdot D} \tag{1.10}$$

Where I is the intensity of received signal, I_0 is the intensity of base signal (T_2-weighted), b_{PGSE} is the factor of sensibility (parameters of PGSE sequence) and D is the coefficient of diffusivity (intrinsic characteristic of the tissue).

$$b_{PGSE} = (\gamma G \delta)^2 (\Delta - \frac{\delta}{3})[s/mm^2] \tag{1.11}$$

Where G is the diffusion gradient intensity, δ is the duration of the diffusion gradient and Δ is the time between the first diffusion and the second.

Figure 1.15

The diffusion can be affected even to pressure, temperature and molecular interactions and the DW-MRI can not distinguish between these different causes. Furthermore, if the followed path during the diffusion is random rather than linear, the signal will be only a measure between the starting point and the end point 1.16. For these reasons the D is not correct and should be replaced by a coefficient called *apparent diffusion coefficient* (ADC)

$$I = I_0 \cdot e^{-b_{PGSE} \cdot ADC} \tag{1.12}$$

Figure 1.16

In the brain, the diffusivity of the water molecules is *anisotropic*, it is not equal in each direction of the space. For example the diffusion in the white matter will be higher along the direction of the axons rather than the perpendicular direction. While, if the diffusion does not have any preferential direction, such as in the CSF, the diffusion is called *isotropic* 1.17. In this case the Stejskal-Tanner equation becomes:

$$I = I_0 \cdot e^{-b_{PGSE} \cdot \hat{g}^T \mathbf{D} \hat{g}} \tag{1.13}$$

Figure 1.17

1.2.2 Diffusion Tensor Imaging (DTI)

One of the most popular and widely used mathematical models to describe the primary orientation of white math axonal path is called *diffusion tensor imaging*. This model was introduced in 1994 [Basser et al., 1994] and it consists of estimating an effective *diffusion tensor* (**D**) within a voxel, which allows to represent its properties with a 3D ellipse. The diffusion tensor is described by a 3x3 symmetric tensor that uses 6 PGSE sequences, one for each different orientation of diffusion gradient, because $D_{yx} = D_{xy}$, $D_{zx} = D_{xz}$ and $D_{zy} = D_{yz}$.

$$\mathbf{D} = \begin{pmatrix} D_{xx} & D_{xy} & D_{xz} \\ D_{yx} & D_{yy} & D_{yz} \\ D_{zx} & D_{zy} & D_{zz} \end{pmatrix} \tag{1.14}$$

Using the eigendecomposition of **D** are computed the eigenvectors and eigenvalues used to represent an ellipse on 3 orthogonal directions 1.18. The eigenvalues λ_i are the likelihoods of diffusion direction of a voxel. The largest eigenvalue(λ_1) is the principal direction of axons in that voxel.

$$\mathbf{D} = \mathbf{Q}\boldsymbol{\Lambda}\mathbf{Q}^{-1}$$

$$\boldsymbol{\Lambda} = \begin{pmatrix} \lambda_1 & 0 & 0 \\ 0 & \lambda_2 & 0 \\ 0 & 0 & \lambda_3 \end{pmatrix} \tag{1.15}$$

Figure 1.18

The result from the DW-MRI is difficult to visualize in a single image. In order to sintetize the information, the eigenvalues are used to compute some metrics that characterize each voxel. The most used are the *Mean Diffusivity* (MD) and the *Fractional Anisotropy* (FA) and they are computed by the $Trace$ of the diffusion matrix.

$$MD = \frac{Tr(D)}{3} = \frac{\lambda_1 + \lambda_2 + \lambda_3}{3} \tag{1.16}$$

$$FA = \sqrt{\frac{3}{2}} \frac{\sqrt{(\lambda_1 - MD)^2 + (\lambda_2 - MD)^2 + (\lambda_3 - MD)^2}}{\sqrt{\lambda_1^2 + \lambda_2^2 + \lambda_3^2}} \tag{1.17}$$

The MD is proportional to the $Trace$ and it quantify the amplitude of the ellipse, or how much a particle is freely to move. Therefore, the MD does not have any information about the directions, but on how much free water is contained into a voxel. The FA is a metric between 0 and 1 and it measures the degree of anisotropy in a voxel. More the diffusion directions are equal more the FA tends to 0. On the other and, an anisotropic diffusion will have a value of 1.

Other metrics are the *Axial Diffusivity* (AxD) and the *Radial Diffusivity* (RD). The Axial diffusivity is the diffusivity along the principal axis of the diffusion ellipsoid.

While the Radial diffusivity is a measure used to express the diffusivity perpendicular to the principal direction of diffusion.

$$AD = \lambda_1 \tag{1.18}$$

$$RD = \frac{\lambda_2 + \lambda_3}{2} \tag{1.19}$$

Both FA and MD can be represented on *diffusion direction maps*. The CSF will have an high MD since the water is free to move in all the directions, while the WM will have an high FA because oriented along a single direction. The image obtained from FA is called *FA map* and often they are displayed as *RGB FA maps*, in which colors are used to represent the principal direction of the diffusion (Red: left-right; Green: anterior-posterior; Blue: superior-inferior) 1.19.

Figure 1.19

Limitations of DTI

The main limitation of DTI model is that water molecules follow a Gaussian distribution. Therefore, only a bundle of fibers can be modeled inside each voxel, but in reality a complex organization of fibers is observed in every voxel. For example, a voxel containing two crossing fibers is modeled by a large diffusion tensor rather than two narrow tensors. Therefore in these voxel, the DTI model does not hold the assumption of a Gaussian distribution, and the resulting FA or MD metrics do not reflect the actual anatomical microstructure 1.20.

Figure 1.20

1.2.3 Tractography

1.3 DW-MRI Microstructural models

1.3.1 NODDI

Dendrites and axons, known collectively as neurites, are the cellular building blocks of the computational circuitry of the brain. Quantifying neurite morphology in terms of its density and orientation distribution provides a view between normal populations and populations with brain disorder. [Zhang et al., 2012] Neurite Orientation Dispersion and Density Imaging (NODDI) is a three-compartment tissue model that models the microstructure complexity of dendrites and axons. Such indices of neurites provide more specific markers of brain tissue microstructure than DTI. [Zhang et al., 2012]

NODDI distinguishes three types of microstructural environment: intra-cellular, extra-cellular and CSF compartments. Each gives to a separate normalized MR signal A_i combined as

$$A = (1 - \nu_{iso})(\nu_{ic}A_{ic} + (1 - \nu_{ic})A_{ec}) + \nu_{iso}A_{iso} \tag{1.20}$$

where A_{ic}, A_{ec}, A_{iso} and ν_{ic}, ν_{iso} are the normalized signal and volume fraction of intra-cellular, extra-cellular and CSF compartments respectively.

Figure 1.21

The *intra-cellular* compartment refers to the space bounded by the membrane of neurites. This space is modeled by cylinders of zero radius (*stiks*), and their orientation distribution can range from higly parallel to highly dispersed. The orientation distribution function is modeled with a *Watson distribution* 1.22:

Figure 1.22

$$f(\mathbf{n}) = M(\frac{1}{2}, \frac{3}{2}, \kappa)^{-1} e^{\kappa(\mu \mathbf{n})^2} \tag{1.21}$$

where M is a confluent hypergeometric function, μ is the mean orientation, and κ is the concentration parameter that measure the extent of orientation dispertion about μ. The normalized signal, A_{ic}, is expressed as follows:

$$A_{ic} = \int_{\mathbb{S}^2} f(\mathbf{n}) e^{-bd_{\|}(\mathbf{q}\cdot\mathbf{n})^2} \, d\mathbf{n} \tag{1.22}$$

where $\mathbf{q}$ and b are the gradeint direction and b-value of diffusion-weighting, $f(\mathbf{n})d\mathbf{n}$ gives the probability of finding stiks along orientation $\mathbf{n}$. $e^{-bd_{\|}(\mathbf{q}\cdot\mathbf{n})^2}$ gives the signal attenuation due to unhindered diffusion along a stick with intrinsic diffusivity $d_{\|}$ and orientation $\mathbf{n}$.

The *extra-cellular* compartment refers to the space around the neurites which is occupied by varius types of glial cells and additionally gray matter and cell bodies [Zhang et al., 2012]. The diffusion motion is modeled by a Gaussian anisotropic distribution and the normalized signal is modeled with a tensor since the perpendicular dissusivities are taken in account:

$$\log A_{ec} = -b\mathbf{q}^T (\int_{\mathbb{S}^2} f(\mathbf{n}) D(\mathbf{n}) \, d\mathbf{n}) \mathbf{q} \tag{1.23}$$

where $D(\mathbf{n})$ is the diffusion tensor with the principal diffusion direction $\mathbf{n}$, diffusion coefficients $d_{\|}$ and $d_{\perp}$ parallel and perpendicular to $\mathbf{n}$ respectively. The perallel diffusivity ($d_{\|}$) is the same as the intrinsic free diffusivity of the intra-cellular compartment, while the perpendicular diffusivity ($d_{\perp}$) is set as $d_{\perp} = d_{\|}(1 - \nu_{ic})$.

The CSF compartment models the space occupied by cerebrospinal fluid and is model as isotropv Gaussian diffusion with diffusivity d_{iso}.

$$A_{ios} = e^{-bd_{iso}} \tag{1.24}$$

Model parameters

The complete set of parameters for the NODDI model is composed by: intra-cellular volume fraction (ν_{ic}) also called *Neurite Density Index* (NDI), parallel diffusion coefficient ($d_{\|}$), concentration parameter of Watson distribution (κ), mean orientation of Watson distribution (μ), isotropic volume fraction (ν_{iso}), isotropic diffusivity (d_{iso}) [Zhang et al., 2012]. The diffusivities are fixed to typical values[7] and the remaining parameter are estimated. Furthermore, it is possible to compute the *Orientation Dispersion Index* (ODI) [Zhang et al., 2011] which is a NODDI's summary statistic for quantifying angular variation of neurite orientation.

$$ODI = \frac{2}{\pi}\arctan(\frac{1}{\kappa}) \tag{1.25}$$

Limitations

NODDI focuses on explicitly modelling the fascicle dispersion with a Watson distribution of sticks in each voxel, but this assumption is inconsistent with the know tissue microstructure: fasciles with various microstructures have been observed in the brain. Furthermore it ignores the intra-axonal radial diffusivity and considers only a single fascicle compartment per voxel, while fascicles crossing with angle $> 40\circ$ occurs in $60 - 90\%$ of the voxels. NODDI can capture crossing fascicles as increased dispersion but cannot characterize each of them separately. [Scherrer et al., 2016]

1.3.2 DIAMOND

The signal arising from a voxel is composed by signals of multiple compartments. Model whose parameters reflect the tissue compartment present in each voxel are called *diffusion compartment models* 1.23. The *DIstribution of 3D Anisotropic MicrOstructural eNvironments in Diffusion-compartment imaging* (DIAMOND) is an hybrid biophysical model of the tissues that combines multicompartment and statistal modelling to provide insight into each compartment in each voxel.[Scherrer et al., 2016]. It is inspired by the statistical framework of [Yablonskiy et al., 2003] but capable to characterize the three-dimensional anisotropy of diffusion observed in the brain and describe the spin packets' distribution of fascicles.

Figure 1.23

DIAMOND requires the estimation of the number of tissue compartments in each voxel, which enables direct assesment of compartments-specific diffusion characteristic such as the compartment mean diffusivitu (cMD), axial diffusivity (cAD) and radial diffusivity (cRD).

The fraction of spin packets described by a 3D diffusivity $\mathbf{D}$ in the voxel is given by a *matrix-variate* distribution $P(\mathbf{D})$. Therefore, if a voxel consisted of exaclty one *homogeneous* microstructural environment characterized by a tensor $\mathbf{D}^0$, then $P(\mathbf{D})$ would

[7] The diffusivities are fixed to respective typical values: $d_{\|} = 1.7 \times 10^{-}3mm^2s^{-1}$ and $d_{iso} = 3 \times 10^{-3}mm^2s^{-1}$

be a delta function $P(\mathbf{D}) = \delta(\mathbf{D} - \mathbf{D}^0)$ and the model would be equivalent to DTI. While, if it consisted of several identifiable homogeneus microstructural eNvironments, a mixture of delta functions would be used [Scherrer et al., 2016] 1.24. Then the DW signal S_k is modeled by:

$$S_k = S_0 \int_{\mathbf{D} \in Sym^+(3)} P(\mathbf{D}) \exp(-b_k \mathbf{g}_k^T \mathbf{D} \mathbf{g}_k) \, d\mathbf{D} \tag{1.26}$$

where $Sym^+(3)$ is the set of 3x3 SPD[8] matrices, $\mathbf{g}_k$ is the orientation of the diffusion gradient and b_k is the b-value of the sequence.

Figure 1.24

More realistically each microstructural environment contain some degree of *heterogeneity* and is best described by a *population of spin packets*. To reach this by modelling each population with a peak-shaped matrix-variate distribution centred in D^0 1.25. DIAMOND uses a *matrix-variate Gamma* (mv-Γ) distribution with *shape parameter* $\kappa > \frac{p-1}{2}$ and *scale parameter* $\Sigma \in Sym^+(3)$ [Scherrer et al., 2016].

$$P_{\kappa,\Gamma}(\mathbf{D}) = \frac{|\mathbf{D}|^{\kappa-(p+1)/2}}{|\Sigma|^{\kappa} \Gamma_p(\kappa)} \exp(-trace(\Sigma^{-1}\mathbf{D})) \tag{1.27}$$

where $|\cdot|$ is the matrix determinant and Γ_p is the multi-variare gamma function. It's expectation is $\mathbf{D}^0 = \kappa\Sigma$, and the shape parameter κ determines the concentration of the densisty around the mean value $\mathbf{D}^0$. An heterogeneity index ($cHEI$) can be computed following the same transform as ODI in NODDI [Zhang et al., 2012]: $cHEI(\kappa) = 2/\pi \arctan(1/\kappa)$.

Considering N_p populations each of them with a mv-Γ distribution $P_{\kappa_j,\Sigma_j}(\mathbf{D})$ with $j \in [1, ..., N_p]$ the matrix-variate distribution is defined as [Scherrer et al., 2016]:

$$P(\mathbf{D}) = \sum_{j=1}^{N_p} f_j P_{\kappa_j,\Sigma_j}(\mathbf{D}) \tag{1.28}$$

where f_j are the occupation fractions and $\sum_{j=1}^{N_p} f_j = 1$.

Figure 1.25

Combining 1.26 and 1.28 and using the Laplace transformation, the following model is found [Scherrer et al., 2016]:

$$S_k = S_0 \sum_{j=1}^{N_p} f_j \mathcal{D}(\mathbf{D}_j^0, \kappa_j) \tag{1.29}$$

where $\mathcal{D}(\mathbf{D}^0, \kappa) = S_0(1 + \frac{b_k \mathbf{g}_k^T \mathbf{D}^0 \mathbf{g}_k}{\kappa})^{-\kappa}$.

[8]SPD: symmetric positive-definite matrices 3x3

Limitations

To summarise, DIAMOND focuses on capturing the distribution of 3D diffusivities arising from each tissue compartment (*model of the tissues*), and in constrast of the *model of the signal*, it requires the estimation of the number of tissue compartments (N_p) in each voxel, that is, the number of mv-Γ components. The estimation of N_p could be the only limitation of this model.

1.3.3 Microstructure fingerprinting

Microstructure fingerprinting is a model which leverages Monte Carlo simulation for the estimation of physically interpretable microstructural parameters, both in single and in crossing fascicles of axons in each voxel [Rensonnet et al., 2019]. It is a multicompartment model as DIAMOND, each voxel is composed of different structures. Monte Carlo simulations of DW-MRI signals, or *fingerprints*, are pre-computed for a large collection of microstructural configurations. At every voxel, the microstructural parameters are estimated by optimizing a spase combination of the fingerprints [Rensonnet et al., 2019].

MF is based of the *superposition principle* of crossing fascicles 1.26, it assumes that the DW-MRI signal S of each voxel is composed by independent contributions of K fasciles of axons with different orientations $\mathbf{u}_k$ occupying fractions ν_k of the physical volume and of a partial volume ν_{CSF} of cerebrospinal fluid [Rensonnet et al., 2019]. S can be espressed as:

$$\begin{aligned} S &= M_0 \left[\sum_{k=1}^{K} \nu_k A_{fasc}(\,\boldsymbol{\Omega}_k, \mathbf{T}_k, \mathbf{u}_k; \mathbf{g}) \,+ \nu_{csf} A_{csf}(\,D_{csf}, \mathbf{T}_{csf}; \mathbf{g}) \right] \\ &= \sum_{k=1}^{K} w_k A_k + w_{csf} A_{csf} \end{aligned} \tag{1.30}$$

where M_0 is the initial transverse magnetization of the voxel, $A_k := A_{fasc}(\,\boldsymbol{\Omega}_k, \mathbf{T}_k, \mathbf{u}_k; \mathbf{g})$ is the normalized DW-MRI signal of the k-th fascicle, modeled by a Monte Carlo simulation, that would arise from an environment composed of fasciles with parameters $\boldsymbol{\Omega}_k$ and $\mathbf{T}_k$, and w_k is its weight defined as 1.31. Water is assumed to diffuse freely and isotropically with a scalar diffusivity D_{csf}.

$$w_k = M_0 \nu_k \iff \nu_k = \frac{w_k}{\sum_{k=1}^{K+1} w_k} \tag{1.31}$$

Figure 1.26

The dictionary is composed of DW-MRI signals (*fingerprints*) obtained by Monte Carlo simulations of the random walk of water molecules in environments defined by *hexagonal packing of impermeable cylinders* with different microstrucutral parameters Ω_k that rapresent the axons [Rensonnet et al., 2019]. The fasciles are modeled by an axonal radius (r) and separation between the cylinders (s).
Fascicle can be described by its intra-axonal volume fraction (or fiber volume fraction fvf), defined as ratio between the area of axons within the hexagon and the area of

Figure 1.27

the hexagon 1.32, and by extra-axonal diffusivity D_{ex}.

$$fvf_{fasc} = \frac{A_{axons \subset hexagon}}{A_{hexagon}} = \frac{2\pi}{\sqrt{3}} \left(\frac{r}{s}\right)^2 \tag{1.32}$$

A canonical dictionary along the orientation $k = 0$, $C^0 = [A_1^0 \dots A_N^0] \in \mathbb{R}^{M \times N}$ is composed by concatenation of all the combinations of the possible fingerprints (fvf and D_{ex}). [Dessain et al., 2022]

After pre-computing the canonical dictionary, the optimal combination of configurations is found at runtime. The runtime method consist in concatenating all the rotations of C_0 along each population and then solving a *sparse optimization problem* to find the best combination of fingerprint and orientation. The sparisty constraint ensure that only one fascicle is chosen out of all possible fascicle for a specific orientation [Rensonnet, 2019]. The sparsity constraint problem can be defined as:

$$(\hat{j}_1, \dots, \hat{j}_K) = \underset{1 \le j_1, \dots, j_K \le N}{\operatorname{argmin}} \min_{\mathbf{w} \ge 0} \left\| \mathbf{y} - \left[\mathbf{A}_{j_1}^1 | \dots | \mathbf{A}_{j_K}^K | \mathbf{A}_{csf}\right] \cdot \begin{bmatrix} w_1 \\ \vdots \\ w_K \\ w_{csf} \end{bmatrix} \right\| \tag{1.33}$$

where $\mathbf{y}$ is the measured signal, and $\mathbf{A}_{j_k}^k = \{A_{fasc}(\Omega_{j_k}, \mathbf{T}_k, \mathbf{u}_k; \mathbf{g}_i(t))\}_{i=1}^M, 1 \le j_k \le N$ is the signal from of a fascile with orientation u_k and microstructural parameters defined with index j. Finally, $\hat{j}_k$ is the index of the optimal fingerprint in the k-th direction.
From the optimal fingerprints and the weights is possible to extract the metrics by:

$$\nu_k = \frac{w_k}{(w_k + w_k)};\ fvf_k = fvf_{\hat{j}_k};\ D_{ex,k} = D_{ex,\hat{j}_k}$$

Limitations

The use of the single scalars r and s to characterize the intra-axonal signal and the assumption on the impermeability of them is an overestimation of axons. Furthermore, the sparsity constraints do not allow mixtures of fingerprints to reconstruct the signal arising from a single fascicle of axons, this could be a limitation for fascicles with differrent microstructural properties in different sub-regions. [Rensonnet, 2019]

Chapter 2

Epilepsy

2.1 Overview of Epilepsy

Epilepsy is a disorder of the brain characterized by a lasting predisposition to generate spontaneous epileptic seizures, and has a numerous neurobiological, cognitive, and psychosocial consequences [Fisher et al., 2014]. Epilepsy affects over 50 million people worldwide, making it one of the most common neurological diseases globally [WHO, 2023]. Over 75% of those with active epilepsy are untreated [Saxena and Li, 2017].

Epilepsy incidence is bimodally distributed with two peaks: the first in the pediatric population less than 5 years old, and the second in people over the age of 50 years. The incidence is higher in low-income countries than high-income countries, thanks a contribution of poor hygiene, poor basic sanitation and higher risk of infection [Thijs et al., 2019]. Regardless the geographical location, the prevalence of active epilepsy is usually between 4 and 12 per 1000, with a risk factor that varies with age [Fiest et al., 2017].

The risk of death for a person with epilepsy is increased compared with the risk for the general population. Mortality in epilepsy can be divided into direct (eg, status epilepticus, injuries, SUDEP [Langan et al., 2000]) or indirect (eg, suicide, drowning) disease-related death [Devinsky et al., 2016].
SUDEP (Sudden Unexpected Death in Epilepsy) is one of the causes of epilepsy-related death, it refers to a death in a patient with epilepsy that is not due to trauma, drowning, status epilepticus, or other known causes but for which there is often evidence of an associated seizure [Nashef, 1997]. The rate of SUDEP increases with the duration and severity of epilepsy, and most cases happen during or right after a seizure [Devinsky, 2011].

Epilepsy rarely stands alone and the presence of comorbidities is the norm: more than 50% of people with epilepsy have one or several additional medical problems [Thijs et al., 2019]. These comorbidities not only include include psychiatric conditions (e.g. depression, anxiety disorder, psychosis, autism spectrum disorder, dementia), but even somatic conditions (e.g. type 1 diabetes, arthritis, digestive tract ulcers) [Yuen et al., 2018].

Definitions

Epilepsy

The given definition of Epilepsy is usually practically applied as having two unprovoked seizures occurring more than 24h apart. But the International League Against Epilepsy (ILAE) proposed that epilepsy be considered to be a disease of the brain by any of the following conditions: [Fisher et al., 2014]

- At least two unprovoked seizures occurring more than 24h apart;
- A single unprovoked seizure if recurrence risk is high (>60% over the next 10 years);
- Diagnosis of an epilepsy syndrome.

Seizure

An epileptic seizure is the clinical manifestation of an abnormal, excessive, purposeless and synchronized electrical discharge in the neurons, that leads to brief episodes of involuntary movement that may involve a part of the body (partial) or the entire body (generalized) and are sometimes accompanied by loss of consciousness and control of bowel or bladder function. [WHO, 2023]

Pathophysiology

A seizure can be conceptualized as occurring when there is a distortion of the normal balance between excitation and inhibition within a neural network [Fisher et al., 2005].

In focal epilepsies, focal functional disruption results in seizures beginning in a localized fashion in one hemisphere, commonly limbic or neocortical, which then spread by recruitment of other brain areas. The site of the focus and the speed and extent of spread determine the clinical manifestation of the seizure [Duncan et al., 2006, Fisher et al., 2017]. For generalized epilepsies, epileptogenic networks are widely distributed, involving thalamocortical structures bilaterally [Fisher et al., 2017].

The imbalance between excitation and inhibition resulting in epileptogenic networks is not necessarily only an increase of excitation or a loss of inhibition; an aberrant increase in inhibition can also be pro-epileptogenic in some circumstances, such as absence seizures [Pinault and O'brien, 2005] or limbic epilepsies in the immature brain. [Galanopoulou, 2008]

Types of epilepsy

Classification is made at three levels: seizure type, epilepsy type, and epilepsy syndromes. [Fisher et al., 2017]

Seizure type

Seizures are first classified by onset as either focal, generalized or unknown 2.1.

- Focal Onset: Usually limited to a specific region of the brain, called the focus. Level of awareness subdivides focal seizure in those with retained awareness and impaired awareness. Retained awareness means that the person is aware of self and environment during the seizure, even if immobile. In addition, focal seizures are sub-grouped as those with motor and non-motor manifestation.

- Generalized Onset: Affects most or all of the brain. Typically congenital and occurs simultaneously in both hemispheres of the brain. They are almost always accompanied by impaired awareness. Generalized seizures are divided into motor and non-motor (absence) seizures.

- Unknown: It is the case in which the onset is missed or obscured.

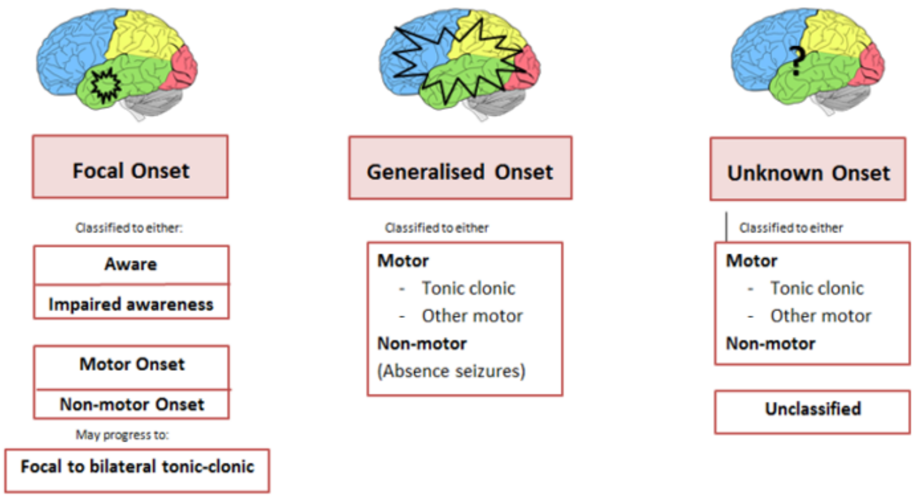

Figure 2.1: The International League Against Epilepsy.[Scheffer et al., 2017]

Epilepsy type

Epilepsies are divided into: focal, generalized, combined generalized and focal, and unknown 2.2. The category combined epilepsy is used for those presenting both seizure types.

Causes of epilepsy

Epilepsy can have both genetic and acquired causes, with the interaction of these factors in many cases. Established acquired causes include serious brain trauma, stroke, tumours, and brain problems resulting from a previous infection.

Treatments

For most of the people with epilepsy Antiepileptic Drug(AEDs) constitute the first line treatment. However, it has been reported that AEDs are effective in only 60-70% of individuals, a percentage that is further reduced in low-income countries. [Duncan et al., 2006].

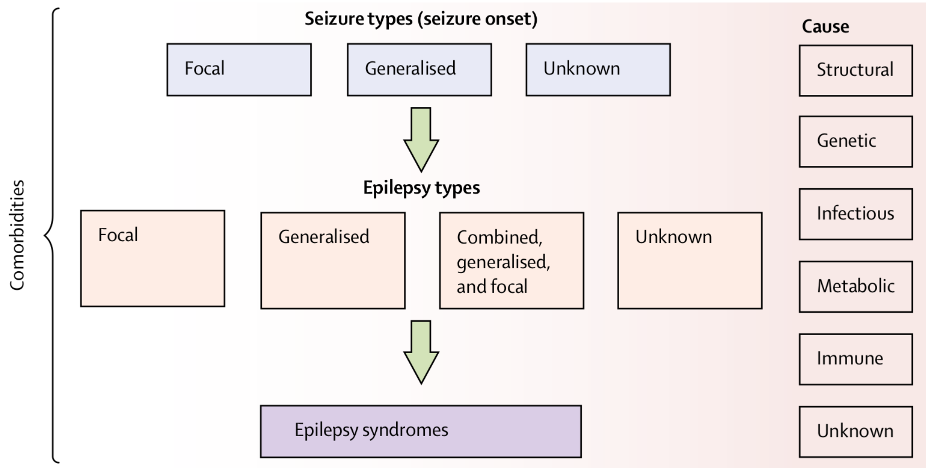

Figure 2.2: The International League Against Epilepsy.[Thijs et al., 2019, Fisher et al., 2017]

Up to a third of all individuals with epilepsy are refractory to AEDs [Spencer and Huh, 2008]. Drug-resistant epilepsy is assumed after the "failure of adequate trials of two tolerated, appropriately chosen and used at correct dosage antiseizure drug schedules to achieve sustained seizure freedom" [Kwan et al., 2010]. In those cases alternative non-pharmacological treatments including surgery and neurostimulatory interventions should be considered. When surgery is not possible because of the presence of multifocal or generalized epilepsy or whenever the epileptogenic focus lies in eloquent cortex that cannot removed, neurostimulation techniques are palliative options [Englot et al., 2013].

Three neurostimulation devices are approved by the Food and Drug Administration (FDA) for the treatment of drug resistant epilepsy [Kiriakopoulos et al., 2018, Wong et al., 2019].

- VNS is approved for treatment of epilepsy when surgery is not possible or does not work. It is not a brain surgery and it is placed under skin on the top left section of the chest and uses wire coils to connect to the left Vagus nerve, located in your neck. It send intermittent electrical continuously. The response rate after a year is 55%.

- RNS is a device that can record seizure activity directly from the brain and delivers stimulation to stop seizures. RNS is implanted near the seizure focus and is flush with the skull, it connects to electrodes that are placed inside your brain. It delivers pulses only when detects abnormal activity in the seizure focus. RNS is not compatible with RNS. The response rate after a year is 45% and grows till 60% in long-term.

- DBS sends signals to the brain electrode to stop signals that trigger a seizure. The connected DBS electrodes are typically placed inside the thalamus, and the electrical pulses are delivered constantly or not. The response rate after a year is 45% and rise till 74% in long-term. Side effects include depression and memory.

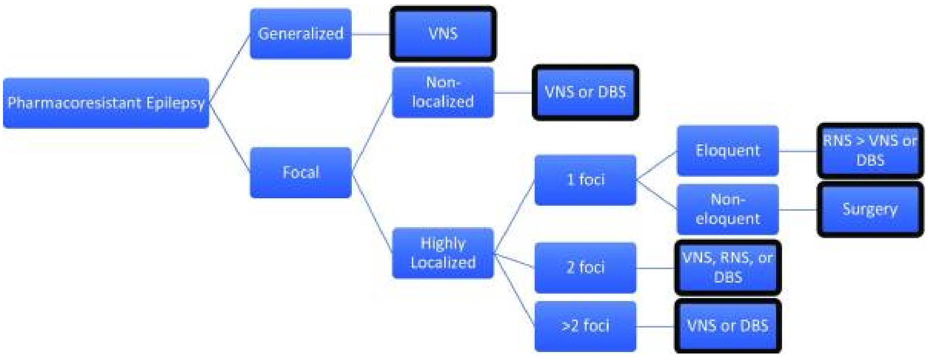

Figure 2.3: The following shows a general algorithm for efficacious device selection based on mechanism of action and focality. Other considerations (side effects, device features, and patient preferences) also drive device selection but are not captured in this flowchart. [Wong et al., 2019]

2.2 Vagus Nerve Stimulation

Vagus Nerve Stimulation (VNS) showed positive effects in multiple other medical conditions, including essential tremors gastroparesis [Krahl et al., 2004], chronic tinnitus, stroke, post-traumatic stress disorder [Hays et al., 2013], chronic pain, Parkinson's disease, eating disorders, multiple sclerosis, migraine and Alzheimer's disease [Broncel et al., 2020, Beekwilder and Beems, 2010].

VNS was implanted first time in four epilepsy patients by Penry and Dean in 1988 [Penry and Dean, 1990]. After several large clinical studies, it was approved for seizures by the European Community in 1994 and FDA in 1997. Clinical trials demonstrate that 24 to 48 months after the implantation of the device, 60% of patients were considered as responders and 8% of implanted patients became seizure free [Englot et al., 2016]. Responders to VNS will be defined as those who experience 50% or greater reduction in seizure frequency after VNS [Ibrahim et al., 2017]. Although VNS is used in clinical practice the exact mechanistic of its effect in modulating seizures remain poorly understood.

VNS consists of a device implanted in the upper left thoracic region with a helical electrode placed around the left cervical nerve, which delivers intermittent electrical impulses to activate the vagus nerve 2.4. Studies in the dog show that right-sided VNS results in a greater degree of bradycardia as compared to the left-sided VNS, because right vagus nerve innervates more densely in the heart [Ardell and Randall, 1986]. Because on those studies VNS is indicated for use only in stimulating the left vagus nerve.

Side effects of VNS are commonly limited to coughing and/or hoarseness of the voice. In a study, voice alternation was reported in 66% of patients on high stimulation and in 30% on low stimulation and cough was reported in 45% of patients. [Ben-Menachem, 2001] To avoid cardiac side effects, a cuff electrode in most cases is implanted on the left vagal nerve.

Vagus Nerve Anatomy and Connections

The vagal nerve (VN) is the longest cranial nerve and exerts a wide range of effects on the body. It comprises two nerves, the left and right vagus nerves and comprises both sensory and motor fibers. The vagal nerve is a mixed nerve made up of 75% sen-

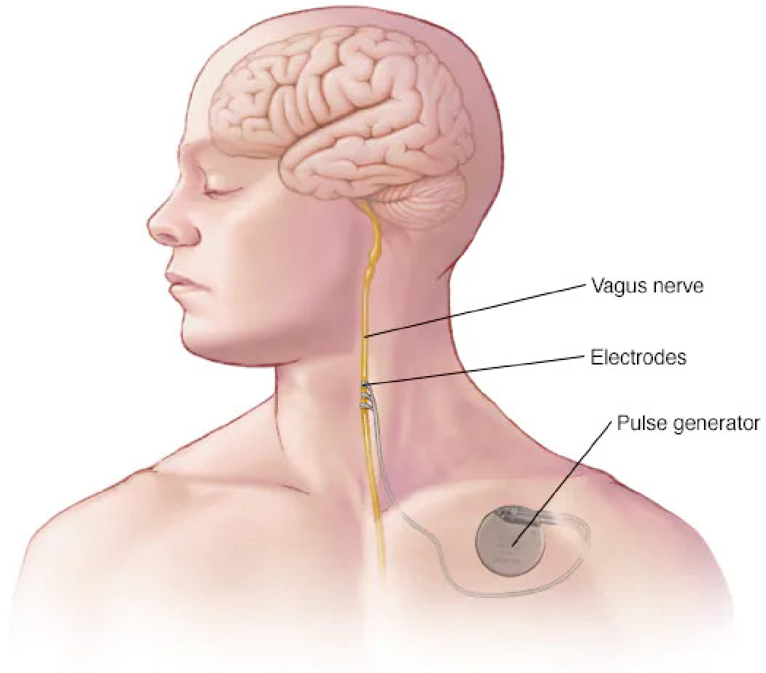

Figure 2.4: Components of the VNS system.

sory(afferent) fibers responsible for the side effects observed (e.g. coughing, difficulties od swallowing, voice modification effects), and 25% efferent fibers which mainly send feedback from heart, lungs, stomach and upper bowel. [Bonaz et al., 2017].

The majority of vagus nerve fibers are comprised of afferents and project to the nucleus tractus solitarius (NTS), which in turn sends fibers to other brainstem nuclei important in modulating the activity of subcortical and cortical circuitry. This vagus afferent network (VagAN) is thought to be the neural substrate of VNS efficacy [Hachem et al., 2018]. The NTS receives direct inputs from the VN and projects to others brainstem nuclei: the locus coeruleus (LC), dorsal raphe nucleus (DRN), and parabranchial nucleus (PBN) [Ricardo and Tongju Koh, 1978]. The functional importance of NTS connectivity in modulating seizure activity is further borne out by findings in rats that increased inhibitory gamma-aminobutyric acid (GABA) signaling or decreased excitatory glutamate signaling within the NST, reduces the susceptibility to chemically induced limbic motor seizures [Walker et al., 1999].

The LC is characterized by widely diffused projections to both subcortical and cortical structures. The projections of the LC are small unmyelinated fibers, forming a wide antero-posterior branching network to reach the raphe nuclei, the cerebellum, and almost all areas of the midbrain and forebrain regions. The LC is the main source of norepinephrine (NE) in the brain [Aghajanian et al., 1977]. NE is a neurotransmitter that has been associated with the clinical effects of VNS by preventing seizure development and by inducing long-term plastic changes that could restore a normal function of the brain circuitry. Indeed, short bursts of VNS increase neuronal firing in the LC, leading to elevations in NE concentrations. [Berger et al., 2021]

Studies have demonstrated indirect projection of the LC to the DRN, which sends

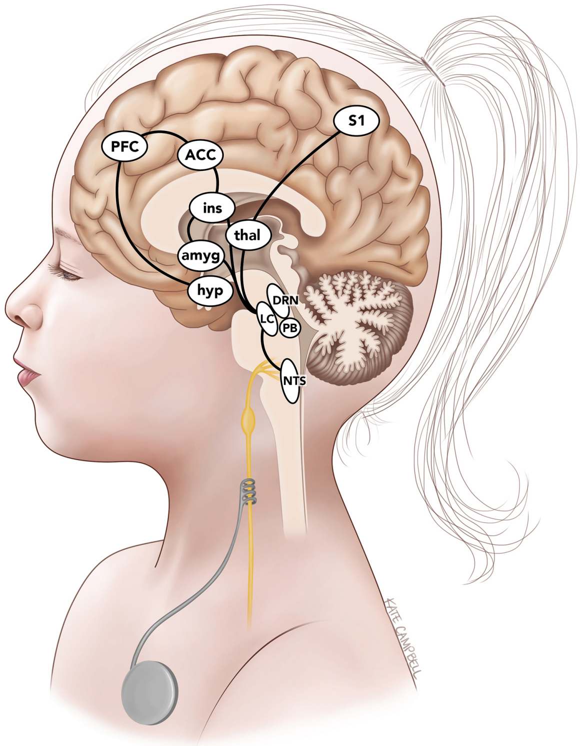

Figure 2.5: The vagus afferent network. Schematic diagram showing the important brainstem centers and subcortical and cortical structures. [Campbell, , Hachem et al., 2018]

widespread projections to upper cortical regions. DRN appears to have a more delayed response to VNS [Hachem et al., 2018].

Vagal afferents project to the PBN by way of both the NTS and LC. Cell bodies within the PBN send diffuse outputs to forebrain structures including the thalamus, insular cortex, amygdala, and hypothalamus. Moreover, PBN likely plays an important role in regulating thalamocortical circuitry that may be implicated in seizure generation. Specifically, PBN activates the intralaminar nuclei of the thalamus, which in turn relays sensory signals to widespread cortical areas. [Hachem et al., 2018]

The Vagus Afferent Network

Structural and Functional connectivity

Structural connectivity and functional connectivity are two concepts that describe different aspects of brain organization. Structural connectivity refers to the anatomical organization of the brain by means of fiber tracts that connect different brain regions. Functional connectivity refers to the statistical dependence or correlation of neural activity patterns between different brain regions. Structural connectivity is often measured by diffusion magnetic resonance imaging (dMRI). Functional connectivity is often measured by electro-encephalography (EEG) or functional magnetic resonance imaging (fMRI)[1].

The main difference between structural connectivity and functional connectivity is that structural connectivity reflects the physical architecture of the brain, while functional connectivity reflects the dynamic interactions of neural activity. Functional

[1]fMRI is a non invasive neuroimaging technique that detects the changes in blood oxygenation and flow that occur in response to neural activity

connectivity can emerge from direct or indirect structural connections, as well as from external inputs or intrinsic dynamics.

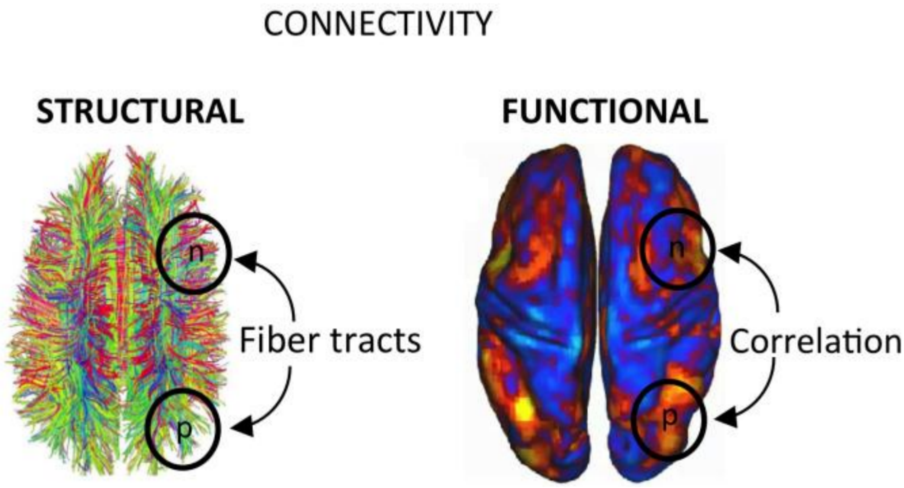

Figure 2.6: Differences between structural and functional connectivity [Cabral et al., 2017].

Thalamocortical Connections

Thalamocortical connections are believed to be an important substrate of VNS responsiveness because they modulate cortical excitability, rendering the brain less susceptible to seizures. The thalamus receives direct inputs from the NTS and PBN [Beckstead et al., 1980]. More recently, thalamic activation measured by BOLD fMRI was associated with improved VNS treatment response in patients with seizures [Narayanan et al., 2002]. The importance of thalamocortical connections in mediating the VNS antiseizure effect is further borne out by a study that utilized resting-state functional MRI (rs-fMRI) data pre-VNS implantation and found an association of greater VNS efficacy with larger connectivity between the thalami to the anterior cingulate cortex (ACC) and left insular cortex [Ibrahim et al., 2017]. Significantly greater FA was observed in VNS (lateralized to the left) responders particularly within anterior and retrolenticular limbs of the internal capsule, anterior, superior and posterior corona radiata, and posterior thalamic radiation. Functional connectivity in MEG also supports the role of intrinsic thalamocortical connectivity in VNS responders, was found that a functional network is significantly more active in VNS responders. [Mithani et al., 2019]

Limbic Circuitry

The limbic system is a collection of neuronal structures involved in controlling emotion, memory, behavior, and motivation. The fornix is the main efferent tract of the hippocampus projecting to the mammillary bodies, nucleus accumbens, septal nuclei, anterior thalamic nuclei and cingulate cortex. While the stria terminalis forms the major input tract from the amygdala to the hypothalamus.

In fornix and stria terminalis, exclusively lateralized to the left, was observed a greater FA in VNS responders. A functional analysis performed by MEG[2] revealed a functional network with significantly greater connectivity in VN responders. These change in the structure and function connectivity imply that the limbic system is involve in an antiseizure action. [Mithani et al., 2019, Mithani et al., 2020]

2.3 Review of DW-MRI in VNS

DTI

In a study of 56 children done by Mithani et al significantly greater FA (within the left size) was observed in VNS responders in the left internal capsule, external capsule, corona radiata, posterior thalamic radiation, fornix and stria terminalis, superior longitudinal fasciculus, inferior longitudinal fasciculus, and inferior front-occipital fasciculus. The mean FA value in these tracts was 0.352 (standard deviation SD = 0.048) in responders and 0.309 (SD = 0.064) in non responders. No significant voxels were observed in the right hemisphere. Furthermore, no statistically significant differences were observed in any other DTI parameters, including MD, radial diffusivity, and axial diffusivity. Healthy controls showed that the profile of responders was more closely related to healthy children than non responders. The mean FA value in significant tracts for matched controls was 0.377 (SD = 0.0274) in healthy controls. [Mithani et al., 2019].

A study conducted on a 4-year-old boy with intractable epilepsy at 10 months after implantation of VNS showed increased FA in the right fimbria-fornix at the level of both cerebral peduncles. [Fan et al., 2014]

[2]Magnetoencephalography: is a functional neuroimaging technique that maps brain activity by recording magnetic fields produced by electrical currents occurring naturally in the brain, using very sensitive magnetometers.

Chapter 3

Methods

3.1 Data

3.1.1 Subjects

3.1.2 Data acquisition

The MRI acquisitions were realized following the *LivaNova guidelines*, requiring the neurostimulators to be turned off during the acquisitions. A trained neurologist used the programming system to set the output current of the device to 0 mA and turn off the sensing before that the patients entered the MRI acquisition room.

Imaging data were acquired using the *SIGNA™ Premier 3T MRI* system (GE Healthcare, Milwaukee, WI, USA), with a transmit-receive 48-channel head coil. T1-anatomical images were acquired using a *Magnetization Prepared - RApid Gradient Echo* (MPRAGE) sequence with the following parameters: $TR = 2186ms$, $TE = 2.95ms$, $FA = 8°$, $TI = 900ms$, bandwidth = $244.14Hz$, matrix size = 256 x 256, 156 axial slices, imaging frequency = $127.77Hz$, voxel size = 1 x 1 x 1 mm^3, acquisition time = 5:26 min.

Diffusion MRI data were acquired with a *Pulsed Gradient Spin Echo* (PGSE) sequence with the following parameters : $TR = 4837ms$, $TE = 80.5ms$ and flip angle = 90°. A multi-shell diffusion scheme was used and was composed of 64 gradients at b = 1000, and 32 gradients at b = 2000, 3000 and 5000 $[s \cdot mm^{-2}]$, interleaved with 7 b0 images. The in-plane FOV was 220 x 220 mm^2 and the data contained 68 axial slices with a $2mm$ thickness (no inter-slice gap, $2mm$ isotropic voxels). A multi-slice excitation scheme was used during the acquisition with a hyperband slice factor of 3 to reduce the acquisition time. The total acquisition time was 13:33 min.

Anatomical files are composed of a NIfTI file (`.nii.gz`) 3.2 containing the measured signal and a JSON file (`.json`) regrouping the acquisition sequence parameters.

Figure 3.1: Anatomical volume slices of a T1 in the sagittal, frontal and axial views

Figure 3.2: Anatomical volume slices of a T2 in the sagittal, frontal and axial views

Diffusion files are composed of a NIfTI file and a JSON file plus two text files (`.bval`) and (`.bvec`) containing the b-values and the b-vectors.

Figure 3.3: Raw diffusion volume slices of a patient for different b-values

3.2 Data preprocessing

3.3 Tractography

3.4 Microstructural analysis

3.5 Statistical analysis

Chapter 4

Results

Chapter 5

Discussion

5.1 Limitations

5.2 Applications

Conclusion and perspectives

Bibliography

[QeA,] Eddy currents.

[Aghajanian et al., 1977] Aghajanian, G., Cedarbaum, J., and Wang, R. (1977). Evidence for norepinephrine-mediated collateral inhibition of locus coeruleus neurons. *Brain Research*, 136(3):570–577.

[Ardell and Randall, 1986] Ardell, J. L. and Randall, W. C. (1986). Selective vagal innervation of sinoatrial and atrioventricular nodes in canine heart. *American Journal of Physiology-Heart and Circulatory Physiology*, 251(4):H764–H773.

[B. Kastler, 1988] B. Kastler, D. V. (1988). *Comprendre l'IRM: Manuel d'auto-apprenissage*. Imagerie médicale DIAGNOSTIC.

[Basser et al., 1994] Basser, P. J., Mattiello, J., and LeBihan, D. (1994). Mr diffusion tensor spectroscopy and imaging. *Biophysical journal*, 66(1):259–267.

[Beckstead et al., 1980] Beckstead, R. M., Morse, J. R., and Norgren, R. (1980). The nucleus of the solitary tract in the monkey: Projections to the thalamus and brain stem nuclei. *Journal of Comparative Neurology*, 190(2):259–282.

[Beekwilder and Beems, 2010] Beekwilder, J. and Beems, T. (2010). Overview of the clinical applications of vagus nerve stimulation. *Journal of clinical neurophysiology*, 27(2):130–138.

[Ben-Menachem, 2001] Ben-Menachem, E. (2001). Vagus nerve stimulation, side effects, and long-term safety. *Journal of clinical neurophysiology*, 18(5):415–418.

[Berger et al., 2021] Berger, A., Vespa, S., Dricot, L., Dumoulin, M., Iachim, E., Doguet, P., Vandewalle, G., and El Tahry, R. (2021). How is the norepinephrine system involved in the antiepileptic effects of vagus nerve stimulation? *Frontiers in Neuroscience*, 15.

[Bonaz et al., 2017] Bonaz, B., Sinniger, V., and Pellissier, S. (2017). The vagus nerve in the neuro-immune axis: Implications in the pathology of the gastrointestinal tract. *Frontiers in Immunology*, 8.

[Broncel et al., 2020] Broncel, A., Bocian, R., Kłos-Wojtczak, P., Kulbat-Warycha, K., and Konopacki, J. (2020). Vagal nerve stimulation as a promising tool in the improvement of cognitive disorders. *Brain Research Bulletin*, 155:37–47.

[Cabral et al., 2017] Cabral, J., Kringelbach, M. L., and Deco, G. (2017). Functional connectivity dynamically evolves on multiple time-scales over a static structural connectome: Models and mechanisms. *NeuroImage*, 160:84–96. Functional Architecture of the Brain.

[Campbell,] Campbell, K. Medical and science illustration, animations and communications.

[Dessain et al., 2022] Dessain, Q., Delinte, N., Macq, B., and Rensonnet, G. (2022). Fast multi-compartment microstructure fingerprinting using deep neural networks. In *Proc. Intl. Soc. Mag. Reson. Med*, volume 30, page 0560.

[Devinsky, 2011] Devinsky, O. (2011). Sudden, unexpected death in epilepsy. *New England Journal of Medicine*, 365(19):1801–1811. PMID: 22070477.

[Devinsky et al., 2016] Devinsky, O., Spruill, T., Thurman, D., and Friedman, D. (2016). Recognizing and preventing epilepsy-related mortality. *Neurology*, 86(8):779–786.

[Duncan et al., 2006] Duncan, J. S., Sander, J. W., Sisodiya, S. M., and Walker, M. C. (2006). Adult epilepsy. *The Lancet*, 367(9516):1087–1100.

[Englot et al., 2013] Englot, D. J., Lee, A. T., Tsai, C., Halabi, C., Barbaro, N. M., Auguste, K. I., Garcia, P. A., and Chang, E. F. (2013). Seizure types and frequency in patients who "fail" temporal lobectomy for intractable epilepsy. *Neurosurgery*, 73(5):838–844.

[Englot et al., 2016] Englot, D. J., Rolston, J. D., Wright, C. W., Hassnain, K. H., and Chang, E. F. (2016). Rates and predictors of seizure freedom with vagus nerve stimulation for intractable epilepsy. *Neurosurgery*, 79(3):345–353.

[Fan et al., 2014] Fan, P.-C., Peng, S. S.-F., Yen, R.-F., Shieh, J.-Y., and Kuo, M.-F. (2014). Neuroimaging and electroencephalographic changes after vagus nerve stimulation in a boy with medically intractable myoclonic astatic epilepsy. *Journal of the Formosan Medical Association*, 113(4):258–263.

[Fiest et al., 2017] Fiest, K. M., Sauro, K. M., Wiebe, S., Patten, S. B., Kwon, C.-S., Dykeman, J., Pringsheim, T., Lorenzetti, D. L., and Jetté, N. (2017). Prevalence and incidence of epilepsy. *Neurology*, 88(3):296–303.

[Fisher et al., 2014] Fisher, R. S., Acevedo, C., Arzimanoglou, A., Bogacz, A., Cross, J. H., Elger, C. E., Engel Jr, J., Forsgren, L., French, J. A., Glynn, M., Hesdorffer, D. C., Lee, B., Mathern, G. W., Moshé, S. L., Perucca, E., Scheffer, I. E., Tomson, T., Watanabe, M., and Wiebe, S. (2014). Ilae official report: A practical clinical definition of epilepsy. *Epilepsia*, 55(4):475–482.

[Fisher et al., 2005] Fisher, R. S., Boas, W. v. E., Blume, W., Elger, C., Genton, P., Lee, P., and Engel Jr., J. (2005). Epileptic seizures and epilepsy: Definitions proposed by the international league against epilepsy (ilae) and the international bureau for epilepsy (ibe). *Epilepsia*, 46(4):470–472.

[Fisher et al., 2017] Fisher, R. S., Cross, J. H., French, J. A., Higurashi, N., Hirsch, E., Jansen, F. E., Lagae, L., Moshé, S. L., Peltola, J., Roulet Perez, E., Scheffer, I. E., and Zuberi, S. M. (2017). Operational classification of seizure types by the international league against epilepsy: Position paper of the ilae commission for classification and terminology. *Epilepsia*, 58(4):522–530.

[Galanopoulou, 2008] Galanopoulou, A. S. (2008). Gabaa receptors in normal development and seizures: friends or foes? *Current neuropharmacology*, 6(1):1–20.

[Hachem et al., 2018] Hachem, L. D., Wong, S. M., and Ibrahim, G. M. (2018). The vagus afferent network: emerging role in translational connectomics. *Neurosurgical Focus FOC*, 45(3):E2.

[Hays et al., 2013] Hays, S. A., Rennaker, R. L., and Kilgard, M. P. (2013). Chapter 11 - targeting plasticity with vagus nerve stimulation to treat neurological disease. In Merzenich, M. M., Nahum, M., and Van Vleet, T. M., editors, *Changing Brains*, volume 207 of *Progress in Brain Research*, pages 275–299. Elsevier.

[Ibrahim et al., 2017] Ibrahim, G. M., Sharma, P., Hyslop, A., Guillen, M. R., Morgan, B. R., Wong, S., Abel, T. J., Elkaim, L., Cajigas, I., Shah, A. H., Fallah, A., Weil, A. G., Altman, N., Bernal, B., Medina, S., Widjaja, E., Jayakar, P., Ragheb, J., and Bhatia, S. (2017). Presurgical thalamocortical connectivity is associated with response to vagus nerve stimulation in children with intractable epilepsy. *NeuroImage: Clinical*, 16:634–642.

[Kennepohl D., 2019] Kennepohl D., Farmer S., S. R. (2019). *Theory of Nuclear Magnetic Resonance (NMR)*, chapter 13. MindTouch.

[Kiriakopoulos et al., 2018] Kiriakopoulos, E., Cascino, G. D., and Britton, J. W. (2018). Types of epilepsy surgery.

[Krahl et al., 2004] Krahl, S. E., Martin, F. C., and Handforth, A. (2004). Vagus nerve stimulation inhibits harmaline-induced tremor. *Brain Research*, 1011(1):135–138.

[Kwan et al., 2010] Kwan, P., Arzimanoglou, A., Berg, A. T., Brodie, M. J., Allen Hauser, W., Mathern, G., Moshé, S. L., Perucca, E., Wiebe, S., and French, J. (2010). Definition of drug resistant epilepsy: Consensus proposal by the ad hoc task force of the ilae commission on therapeutic strategies. *Epilepsia*, 51(6):1069–1077.

[Langan et al., 2000] Langan, Y., Nashef, L., and Sander, J. W. A. S. (2000). Sudden unexpected death in epilepsy: a series of witnessed deaths. *Journal of Neurology, Neurosurgery & Psychiatry*, 68(2):211–213.

[Mithani et al., 2019] Mithani, K., Mikhail, M., Morgan, B. R., Wong, S., Weil, A. G., Deschenes, S., Wang, S., Bernal, B., Guillen, M. R., Ochi, A., Otsubo, H., Yau, I., Lo, W., Pang, E., Holowka, S., Snead, O. C., Donner, E., Rutka, J. T., Go, C., Widjaja, E., and Ibrahim, G. M. (2019). Connectomic profiling identifies responders to vagus nerve stimulation. *Annals of Neurology*, 86(5):743–753.

[Mithani et al., 2020] Mithani, K., Wong, S. M., Mikhail, M., Pourmotabbed, H., Pang, E., Sharma, R., Yau, I., Ochi, A., Otsubo, H., Snead, O. C., Donner, E., Go, C., Widjaja, E., Babajani-Feremi, A., and Ibrahim, G. M. (2020). Somatosensory evoked fields predict response to vagus nerve stimulation. *NeuroImage: Clinical*, 26:102205.

[Narayanan et al., 2002] Narayanan, J., Watts, R., Haddad, N., Labar, D., Li, P., and Filippi, C. (2002). Cerebral activation during vagus nerve stimulation: A functional mr study. *Epilepsia*, 43(12):1509–1514.

[Nashef, 1997] Nashef, L. (1997). Sudden unexpected death in epilepsy: Terminology and definitions. *Epilepsia*, 38(s11):S6–S8.

[O. Rampado, 2017] O. Rampado, M. C. (2017). *Elementi di risonanza magnetica*. Springer.

[Penry and Dean, 1990] Penry, J. K. and Dean, J. C. (1990). Prevention of intractable partial seizures by intermittent vagal stimulation in humans: Preliminary results. *Epilepsia*, 31(s2):S40–S43.

[Pinault and O'brien, 2005] Pinault, D. and O'brien, T. J. (2005). Cellular and network mechanisms of genetically-determined absence seizures. *Thalamus & related systems*, 3(3):181–203.

[Rensonnet, 2019] Rensonnet, G. (2019). In vivo diffusion magnetic resonance imaging of the white matter microstructure from dictionaries generated by monte carlo simulations: development and validation. Technical report, EPFL.

[Rensonnet et al., 2019] Rensonnet, G., Scherrer, B., Girard, G., Jankovski, A., Warfield, S. K., Macq, B., Thiran, J.-P., and Taquet, M. (2019). Towards microstructure fingerprinting: estimation of tissue properties from a dictionary of monte carlo diffusion mri simulations. *NeuroImage*, 184:964–980.

[Ricardo and Tongju Koh, 1978] Ricardo, J. A. and Tongju Koh, E. (1978). Anatomical evidence of direct projections from the nucleus of the solitary tract to the hypothalamus, amygdala, and other forebrain structures in the rat. *Brain Research*, 153(1):1–26.

[Sameer, 2017] Sameer, Q. (2017). Magnetic resonance imaging (mri) in orthopaedics. Last accessed 28 April 2023.

[Saxena and Li, 2017] Saxena, S. and Li, S. (2017). Defeating epilepsy: A global public health commitment. *Epilepsia Open*, 2(2):153–155.

[Scheffer et al., 2017] Scheffer, I. E., Berkovic, S., Capovilla, G., Connolly, M. B., French, J., Guilhoto, L., Hirsch, E., Jain, S., Mathern, G. W., Moshé, S. L., Nordli, D. R., Perucca, E., Tomson, T., Wiebe, S., Zhang, Y.-H., and Zuberi, S. M. (2017). Ilae classification of the epilepsies: Position paper of the ilae commission for classification and terminology. *Epilepsia*, 58(4):512–521.

[Scherrer et al., 2016] Scherrer, B., Schwartzman, A., Taquet, M., Sahin, M., Prabhu, S. P., and Warfield, S. K. (2016). Characterizing brain tissue by assessment of the distribution of anisotropic microstructural environments in diffusion-compartment imaging (diamond). *Magnetic resonance in medicine*, 76(3):963–977.

[Spencer and Huh, 2008] Spencer, S. and Huh, L. (2008). Outcomes of epilepsy surgery in adults and children. *The Lancet Neurology*, 7(6):525–537.

[Thijs et al., 2019] Thijs, R. D., Surges, R., O'Brien, T. J., and Sander, J. W. (2019). Epilepsy in adults. *The Lancet*, 393(10172):689–701.

[Walker et al., 1999] Walker, B. R., Easton, A., and Gale, K. (1999). Regulation of limbic motor seizures by gaba and glutamate transmission in nucleus tractus solitarius. *Epilepsia*, 40(8):1051–1057.

[WHO, 2023] WHO (2023). Epilepsy fact sheet.

[Wong et al., 2019] Wong, S., Mani, R., and Danish, S. (2019). Comparison and selection of current implantable anti-epileptic devices. *Neurotherapeutics*, 16:369–380.

[Yablonskiy et al., 2003] Yablonskiy, D. A., Bretthorst, G. L., and Ackerman, J. J. (2003). Statistical model for diffusion attenuated mr signal. *Magnetic Resonance in Medicine: An Official Journal of the International Society for Magnetic Resonance in Medicine*, 50(4):664–669.

[Yuen et al., 2018] Yuen, A. W., Keezer, M. R., and Sander, J. W. (2018). Epilepsy is a neurological and a systemic disorder. *Epilepsy & Behavior*, 78:57–61.

[Zhang et al., 2011] Zhang, H., Hubbard, P. L., Parker, G. J., and Alexander, D. C. (2011). Axon diameter mapping in the presence of orientation dispersion with diffusion mri. *Neuroimage*, 56(3):1301–1315.

[Zhang et al., 2012] Zhang, H., Schneider, T., Wheeler-Kingshott, C. A., and Alexander, D. C. (2012). Noddi: practical in vivo neurite orientation dispersion and density imaging of the human brain. *Neuroimage*, 61(4):1000–1016.

UNIVERSITÉ CATHOLIQUE DE LOUVAIN
École polytechnique de Louvain
Rue Archimède, 1 bte L6.11.01, 1348 Louvain-la-Neuve, Belgique | **www.uclouvain.be/epl**